Spore-derived porous carbon with tailored heteroatom doping for anode of sodium-ion capacitors

Wang Yiming[1], Qiu Kerou[1], Yu Haidong[2], Hou Zhiqiang[2], Chen Haotian[1], Cheng Jiahao[1], Zhang Yabin[1,*], Zhu Jinliang[1,*], Zou Bingsuo[1]

(1. *Guangxi Key Laboratory of Processing for Non-ferrous Metals and Featured Materials, and School of Resources, Environment and Materials, Guangxi University, Nanning* 530004, *China*;
2. *School of Chemistry and Chemical Engineering, Guangxi University, Nanning* 530004, *China*)

Abstract: Sodium-ion capacitors (SICs) are attractive candidates for low-cost and safe energy storage, but their practical development is limited by the sluggish Na^+ storage kinetics and structural instability of the anodes. Control of both the bulk structure and surface chemistry can address these limitations and achieve fast and durable sodium storage. We report a heteroatom-rich porous carbon (HRPC) produced from spores by hydrothermal pretreatment, low-temperature carbonization, and acid-mediated functionalization. Control of both the pore structure and surface chemistry enables rapid ion/electron transport, improved electrolyte wettability, and abundant Na^+ adsorption sites. Density functional theory calculations show the distinct contributions of different heteroatom configurations to sodium adsorption, providing mechanistic insights into the improved storage behavior. The HRPC anode has an ultrahigh reversible capacity of 446.1 mAh g^{-1} at 50 mA g^{-1}, retaining 237.3 mAh g^{-1} at 2 A g^{-1}, and has an excellent cycling stability. A full SIC assembled with a polyaniline-derived porous carbon cathode has an energy density of 114.4 Wh kg^{-1} at 290 W kg^{-1} and an 84.3% capacity retention after 5000 cycles. This work establishes a scalable and sustainable route for converting biomass into high-value carbon anodes by controlling both the pore structure and surface chemistry, and providing a new way to provide high-performance sodium-ion energy storage.

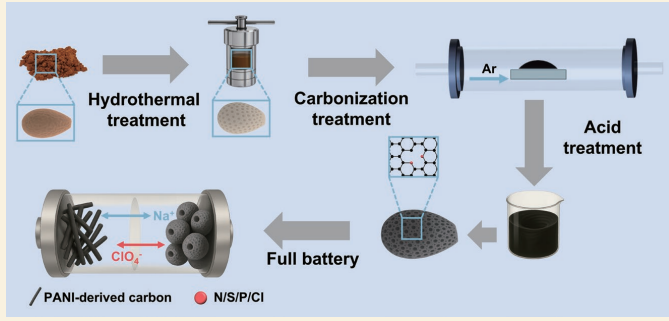

Key words: Spore-derived carbon; Heteroatom doping; Porous structure; Sodium storage ability; Sodium-ion capacitors

1 Introduction

The explosion of the global population has driven an unprecedented surge in the demand for energy, food, and water. However, the excessive reliance on petroleum-based chemicals and fossil fuels has intensified environmental crises, highlighting the urgent need for sustainable and renewable energy sources. Renewable options such as solar, wind, and tidal power have expanded rapidly, yet their inherent intermittency and instability impede deployment at scale. This challenge necessitates the development of efficient electrochemical energy storage (EES) systems capable of ensuring reliable and stable energy supply. Conventional lithium-ion batteries, though widely adopted, face intrinsic limitations including restricted power density, high cost, and safety risks[1]. Supercapacitors (SCs), on the other hand, provide excellent power density and cycling stability but fall short on energy density[2]. To bridge this gap, the concept of alkali metal-ion hybrid capacitors was introduced in 2001. A prototype lithium-ion capacitor synergistically combines the high energy density of battery with the high power density and durability of supercapacitor[3-5]. Yet, the scarcity and high cost of lithium severely constrain the large-scale application of lithi-

Received: March 20, 2026
Revised: April 25, 2026
Accepted: April 27, 2026

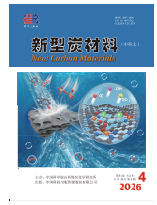

um-ion capacitors (LICs). In view of the natural abundance, low cost, and scalable availability of sodium, sodium-ion capacitors (SICs) were introduced as a promising alternative, offering improvements in terms of safety, energy density, power density, and operating temperature ranges[6–8]. Nevertheless, the large ionic radius of sodium ions compared with lithium introduces substantial challenges, particularly severe volume fluctuations and structural instability in battery-type anodes during sodiation/desodiation. These drawbacks undermine capacity retention, cycling stability, and practical performance. Accordingly, the development of advanced anode materials with high reversible capacity, rapid ion transport kinetics, and robust long-term stability is crucial for unlocking the full potential of SICs and driving their progress toward next-generation energy storage.

Carbonaceous materials are promising for sodium-ion storage due to their low cost, abundance, and excellent thermochemical stability. In particular, biomass-derived carbon materials, obtained from agricultural and forestry wastes such as nut shells[9], straws[10], seeds[11], and wood[12], offer renewable and abundant precursors (~ 550 Gt-C globally). These materials' hierarchical morphology, biogenic elements, and abundant surface functional groups all serve to enable sustainable production of diverse carbons for distinctive charge storage mechanisms and electrochemical behaviors[13–14]. Biomass-derived hard carbons (BDHCs) are especially attractive because their inherent structural defects enhance Na^+ adsorption while amorphous graphene nanodomains enlarge interlayer spacing for efficient intercalation, making it a promising candidates for sodium ion storage with reversible capacities of ~ 300 mAh g^{-1}[15]. Various BDHC architectures, including spherical[16], tubular[17], sheet-like[18], and 3D frameworks[18], have been prepared from diverse biomass sources for excellent sodium-ion storage. However, challenges remain in matching noble metal with oxide-based electrodes, achieving controllable and low-energy-consumption synthesis, and unraveling the underlying mechanisms. Conventional BDHCs synthesis typically requires high temperature (>1300 °C) for carbonization, raising energy costs and limiting scalability[19]. Therefore, research on green and low-cost strategies to fabricate high-performance biomass-derived carbon materials is essential for advancing next-generation sodium-ion storage.

The morphology and surface chemistry of biomass-derived carbon materials play a decisive role in determining electrode and device performance[20]. While direct calcination of biomass precursors with favorable structures and inherent elements under different temperature and time preserves some structural and elemental features[21–23], inherited structure and limited natural content through calcination are limited to further enhance the electrochemical performance. Precise structural and compositional engineering is required to achieve high performance. Well-ordered porous networks facilitate rapid ion diffusion, while surface defects and functional groups enhance capacity[24]. Accordingly, recent efforts have focused on designing pore architectures, surface functionalization, and heteroatom doping. High-temperature alkali activation can yield biochars with hierarchical porosity and large surface area, but it is energy-intensive and environmentally unfriendly, underscoring the need for milder modification strategies[19]. Heteroatom doping introduces defects and functional groups into the carbon frameworks to tailor electron distribution, expand interlayer spacing, and introduce active sites. By introducing elements such as N, S and P, doping tailors electronic distribution, expands interlayer spacing, and creates a multitude of nucleation and redox-active sites, thereby enhancing Na^+ adsorption and storage ability[25]. For instance, nitrogen improves conductivity, wettability, and defect density, enabling efficient Na^+ adsorption and fast kinetics[26]. Sulfur not only widens interlayer spacing through larger atomic size but also introduces redox-active C—S bonds that contribute directly to capacity, though achieving stable S incorporation remains challenging[27–28]. Phosphorus enhances conductivity and Na^+ adsorption through electron donation and lattice expansion[29]. Halogen further polarizes the car-

bon frameworks and modifies charge/spin distribution[30]. More importantly, co-doping or even multiple-doping further synergizes these effects, leading to additional improvements in sodium-ion adsorption, storage capacity, and cycling stability[31–32]. Overall, heteroatom doping is indispensable for achieving high reversible capacity, fast ion transport, and durability in sodium-ion storage. Especially, incorporating higher levels of dopants can greatly enhance sodium storage ability, though conventional doping strategies often face challenges in cost and scalability. As a result, developing low-cost, scalable carbonization and surface-modification strategies to produce structurally customizable biomass carbon materials remains crucial for advancing practical SIC anodes.

Ganoderma lucidum spores (GLS) are a widely recognized biomass precursor for EES devices[22,32–34]. It features inherently robust, double-layered, and porous architectures, primarily composed of chitin-β-glucan complexes enriched with heteroatoms, as demonstrated in our previous work[35–37]. Moreover, GLS can be converted directly into porous carbon materials with high surface area and intrinsic heteroatom doping through calcination. Previous studies have shown that their morphology can be further tuned by hydrothermal treatments to enhance porosity and surface area[38–40]. Building on these structural and compositional advantages, we anticipate that combining its intrinsic porosity with tailored surface functionalization can unlock the full sodium storage potential of GLS-derived carbon materials. To this end, we propose a sustainable strategy to fabricate structurally optimized HRPC anodes through a synergistic process of hydrothermal pretreatment, low-temperature carbonization, and acid-mediated surface functionalization, achieving high-performance sodium-ion storage for next-generation SICs.

In this article, multi-level pore regulation was achieved by hydrothermal treatment at 180 °C. During the process, selective decomposition of the chitin-polysaccharide matrix in the spore wall generated a hierarchically interconnected pore structure while preserving the mechanical integrity of the carbon skeleton. Concurrently, in situ N-doping from endogenous spore components, alongside precise surface chemical regulation, introduced diverse functional groups through various acid treatments. This dual "structure-interface" optimization strategy enhanced electrolyte wettability, improved solid electrolyte interface (SEI) formation, boosted electronic conductivity, and created abundant Na^+ adsorption sites. As a result, the optimized HRPC anode delivered a high specific capacity of 446.1 mAh g^{-1} at 50 mA g^{-1} and excellent cycling stability, retaining 88.9% capacity after 1500 cycles. Furthermore, a full SIC assembled with the HRPC anode and polyaniline-derived porous carbon (PDPC) cathode achieved an impressive energy density of 114.4 Wh kg^{-1} at 290 W kg^{-1}, maintained 84.3% capacity after 5000 cycles at 2.0 A g^{-1}, and exhibited overall electrochemical performance comparable to leading reported SICs.

2 Experimental

2.1 Materials and chemical reagents

Ganoderma lucidum spores were purchased from a cultivation base in Changbai Mountain, Jilin Province, China. Aniline (ANI), ammonium persulfate (APS), potassium hydroxide (KOH) and other reagents were purchased from Aladdin. Concentrated sulfuric acid (H_2SO_4, 98%), hydrochloric acid (HCl, 37%), nitric acid (HNO_3, 70%), and phosphoric acid (H_3PO_4, 85%) were purchased from Nanning Huixin Chemical Glass Instrument Company and used as-is without further purification. Deionized (DI) water were purchased from ULUPURE, China, with a resistivity of 18.2 MΩ and used throughout the experiment.

2.2 Preparation of porous spores

Multi-scale poros spores were prepared through a simple hydrothermal treatment. 1 g of GLS was dispersed in 40 mL of DI water under ultrasonic treatment to form a uniform suspension. The resulting suspension was transferred to a polytetrafluoroethylene-lined stainless-steel autoclave and heated at 180 °C for 24 h. After natural cooling to room temperature, the sample was washed multiple times with ethanol and

with DI water through vacuum filtration (0.22 μm nitrocellulose filter membrane) and then freeze-dried and labelled GLSH for subsequent use.

2.3 Preparation of HRPC

Heteroatom-rich porouscarbon (HRPC) was prepared by a simple low-temperature calcination method. 1 g of GLSH prepared above was placed in an alumina boat and pyrolyzed at 650 °C for 2 h in a tube furnace (Argon atmosphere, flow rate: 40 mL min^{-1}, heating rate: 5 °C min^{-1}). After carbonization, the resulting material was labelled GLSHC. GLSHC was separately immersed in 4 different strong acids (HNO_3, H_2SO_4, H_3PO_4 and HCl), and stirred for 24 h to obtain 4 functionalized samples, which were denoted as GLSHC-HNO_3, GLSHC-H_2SO_4, GLSHC-H_3PO_4, and GLSHC-HCl respectively. Subsequently, the product was filtered and washed with deionized water until the pH reached 7.0. Finally, the obtained HRPC sample was dried in an oven at 60 °C.

2.4 Preparation of PDPC

To prepare polyaniline-derived porous carbon (PDPC), 7.5 g of ANI and 25 mL of 37% HCl were dissolved in 250 mL of DI water. Meanwhile, 4.6 g of APS was dissolved in another 250 mL of DI water containing 25 mL of the same acid. The two solutions were then mixed and stirred for 20 min. The solid product was recovered by filtration, washed, and subsequently freeze-dried for 48 h. Afterwards, the product was pyrolyzed at 600 °C for 1 h under an Ar atmosphere to obtain a carbon material. In the activation step, 0.5 g of the obtained carbon was mixed with 3 g of KOH in water. After removal of water, the dried mixture was heated at 800 °C for 1 h under an Ar atmosphere. The resulting product was washed alternately with diluted HCl and DI water until the pH reached 7, and finally dried in air at 60 °C. The obtained material was labelled PDPC.

2.5 Material characterization

For material characterization, scanning electron microscopy (SEM) analysis was performed using a Hitachi SU8020 high-resolution field emission scanning electron microscope. Transmission electron microscopy (TEM) observations were carried out using a Hitachi HT7700 transmission electron microscope. The samples were also examined by powder X-ray diffraction (XRD) using a Bruker D8 Discover diffractometer (monochromatic Cu $K\alpha_1$ radiation, λ=1.540 59 Å, 40 kV, 30 mA). Raman spectra were recorded using a Renishaw inVia Reflex laser Raman spectrometer (λ=532 nm). X-ray photoelectron spectroscopy (XPS) was carried out on a Thermo Scientific K-Alpha spectrometer (Thermo Fisher Scientific, USA). Fourier transform infrared (FTIR) spectra were acquired with a Thermo Scientific Nicolet iS50 spectrometer (Thermo Fisher Scientific, USA). Electron paramagnetic resonance (EPR) tests were performed on a Bruker EMXplus spectrometer. The porous structure was characterized by nitrogen adsorption and desorption at 77.4 K using a Micromeritics TriStar II 3020 surface area and porosity analyzer. Thermogravimetric analysis (TGA) were conducted on a Shimadzu DTG-60(H) simultaneous thermal analyzer. Contact angle measurements were performed using a POWEREACH contact angle meter with a droplet size of 2 μL each time.

2.6 DFT calculation

Density functional theory (DFT) was used as implemented in the Vienna Ab initio simulation package (VASP) in all calculations. The exchange-correlation potential is described by using the generalized gradient approximation of Perdew-Burke-Ernzerhof (GGA-PBE). The projector augmented-wave (PAW) method is employed to treat interactions between ion cores and valence electrons. The plane-wave cutoff energy was fixed at 450 eV. Given that the structural models were relaxed until the Hellmann-Feynman forces were smaller than -0.02 eV/Å and the change in energy smaller than 1×10^{-5} eV was attained. A 15 Å vacuum layer was added to the surface to eliminate the artificial interactions between periodic images. Grimme's DFT-D3 methodology was used to describe the dispersion interactions among all atoms in adsorption models. The adsorption energy (E_{ads}) of species is calculated by Eq. (1):

$$E_{ads} = E_{(system)} - E_{(catalyst)} - E_{(species)} \quad (1)$$

where $E_{(system)}$, $E_{(catalyst)}$, and $E_{(species)}$ denote the total en-

ergy of the optimized system with adsorbed species, the isolated catalyst, and species, respectively.

2.7 Electrode preparation and battery assembly

To prepare the HRPC anode, the active material, carbon black, and polyvinylidene fluoride (at a mass ratio of 8∶1∶1) were thoroughly mixed. N-methyl-2-pyrrolidone was used as the dispersant. The black slurry was uniformly coated onto a copper foil current collector and then heated under vacuum at 110 °C overnight to evaporate the solvent completely. Subsequently, the coated copper foil was pressed into shape at 5 MPa using a hydraulic press and then punched into circular electrodes with a diameter of 10 mm. The carbon mass loading was 0.8-1 mg. The resulting anode was then heated overnight in a vacuum oven at 160 °C. Finally, the prepared anode and cathode were transferred to an argon-filled glove box for CR2032 coin cell assembly. The half-cell was characterized with the HRPC anode as the working electrode, sodium metal as the counter and reference electrode, with a potential window of 0.01-3.0 V (vs. Na/Na^+). For the HRPC anode, the potential window was selected as 0.01-3.0 V (vs. Na/Na^+), and the full-cell sodium-ion capacitor was assembled with different mass ratios of GLSHC-HNO_3 anode and PDPC, with a potential window of 2.0-4.0 V. Before full-cell assembly, the GLSHC-HNO_3 anode was subjected to 5-10 constant current cycles at a current density of 50 mA g^{-1} within the voltage range of 0.01-3.0 V (vs. Na/Na^+), and finally ended at 3.0 V. The electrolyte was 1 mol L^{-1} $NaClO_4$ dissolved in ethylene carbonate and diethyl carbonate (volume ratio, 1∶1), with 5% (volume fraction) of vinylene carbonate added. A glass fiber membrane (Whatman, UK) was used as the separator.

2.8 Electrochemical measurements

Cyclic voltammetry (CV), galvanostatic charge and discharge (GCD), and electrochemical impedance spectroscopy (EIS) were carried out using a CH760E electrochemical workstation (Shanghai Chenhua Instrument Co., Ltd., China). Rate capability and cycling stability were measured using LAND battery test system (CT2001A, Wuhan LAND Electronic Co., Ltd., China).

Specific capacitance is calculated from GCD data according to the following equation:

$$C_{sp} = \frac{I \times \Delta t}{m \times \Delta V} \tag{2}$$

where C_{sp} (F g^{-1}) denotes tspecific capacitance, I (A) is constant discharge current, Δt(s) is discharge time under constant current, m (g) means mass of the active material, and ΔV (V) is the potential window.

Energy density and power density are calculated using equations:

$$E_{sp} = \frac{1}{3.6} \times \int_{V_1}^{V_2} C_{sp} V \mathrm{d}V \tag{3}$$

$$P_{sp} = \frac{E_{sp}}{\Delta t} \tag{4}$$

where E_{sp} (Wh kg^{-1}) denotes energy density, V_2 (V) is the top potential limit, V_1(V) means the bottom potential limit, P_{sp}(W kg^{-1}) is power density, and Δt (h) is discharge time under a constant discharge current.

3 Results and discussion

3.1 Design and fabrication of HRPC

The desired HRPC was fabricated by a stepwise process (details in Experimental Section) involving hydrothermal pretreatment of GLS, low-temperature carbonization, and subsequent acid functionalization. As illustrated in Fig. 1, the GLS are first hydrothermally treated. Such an initial hydrothermal treatment not only causes the generation of surface pores with small sizes, enabling the expansion of original surface macropores to multilevel pores, but also transform the internal composition of GLS into Chitosan[41]. This structural and component change is attributed to the removal of lipid and the decomposition of biological macromolecules (such as proteins and polysaccharides) inside the GLS under elevated temperature and pressure[42]. The TGA curve (Fig. S1) shows a distinct weight loss plateau for hydrothermally treated GLS in the range of 600-1000 °C, corresponding to the pyrolysis and carbonization of organic components. Weight loss becomes moderate above 700 °C, indicating limited carbonization at higher temperatures. Although higher carbonization temper-

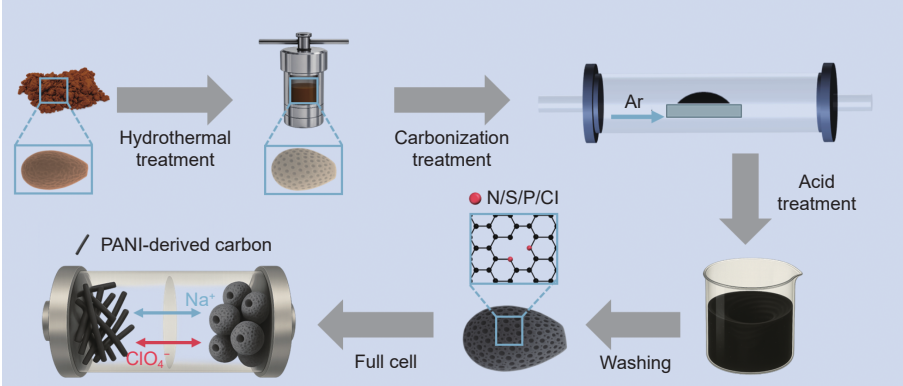

Fig. 1 Schematic illustration of the preparation of HPRC from GLS. HRPC was synthesized by a simple hydrothermal process, low-temperature pyrolysis, and subsequent concentrated acid treatment, and employed as an anode for SICs

atures could improve graphitization and electronic conductivity, they inevitably cause significant loss of heteroatoms (N, S, P), reduction of interlayer spacing, and the collapse of the hierarchical pore structure, all of which are detrimental to Na^+ adsorption and fast storage. Therefore, low-temperature carbonization below 700 °C and the subsquent acid functionalization are expected to preserve as many heteroatom active sites and multiscale pores as possible. In this regard, the hydrothermal GLS (GLSH) was pyrolyzed at 650 °C and thus converted into porous carbons while retaining the porous carbon skeleton structure, denoted as GLSHC. Finally, post-treatment with each of the four different concentrated acids (HNO_3, H_2SO_4, H_3PO_4 and HCl) yielded HRPCs with tailored surface chemistries and heteroatom doping, denoted as GLSHC-*X* (*X* represents the respective acid). This hierarchical fabrication strategy endows HRPC with abundant interconnected pores that enhance electrolyte wettability, while heteroatom incorporation introduces abundant Na^+ adsorption sites. These features act in synergy to boost sodium storage capacity and cycling stability, making HRPC a robust and efficient anode material for SICs.

3.2 Structure characterization and optimization

The morphological evolution of GLS to HRPC during the fabrication was systematically analyzed by SEM (Fig. 2a-c). Consistent with previous publications[35–36], pristine GLS exhibited uniform droplet-like particles (4-7 μm) with surface wrinkles and stomata but possessed a low specific surface area (SSA) of 2.27 $m^2\ g^{-1}$ (Fig. 2i). Such an SSA limits its electrochemical activity, which is important for electrochemical reactions as the electrode material. After 24 h hydrothermal treatment at 180 °C, the formed GLSH retains its droplet-like morphology almost entirely (Fig. 2b) but develops multi-scale concave pits and micropores, modestly increasing surface area to 22.86 $m^2\ g^{-1}$ due to the partial dissolution of chitin-β-glucan complexes resulting in incomplete pore opening. To further improve the structural characteristics of GLSHC to achieve complete pore opening and more efficient ion transport, carbonization at 650 °C subsequently transformed its concave areas into open pores, while partially exposing the hollow cavity (Fig. 2c), resulting in a sharp increase in the surface area (292.82 $m^2\ g^{-1}$). This indicates that carbonization effectively unlocked micropores and expanded accessible surface sites. After undergoing functionalization treatment in concentrated acid, the resultant GLSHC preserves its droplet-like morphology and porous architecture (Fig. S2). Moreover, N_2 adsorption-desorption analysis confirms that the specific surface area remains unchanged (292 $m^2\ g^{-1}$). Mesopore dominance with pore diameters range from 5 to 25 nm (Fig. S4c-d) compared with hydrothermally treated samples. Collectively, these results demonstrate that the sequential hydrothermal-carbonization-acid treatment successfully builds a hierarchical porous framework with high surface area, significantly enhancing electrolyte accessibility and providing abundant active sites for sodium storage.

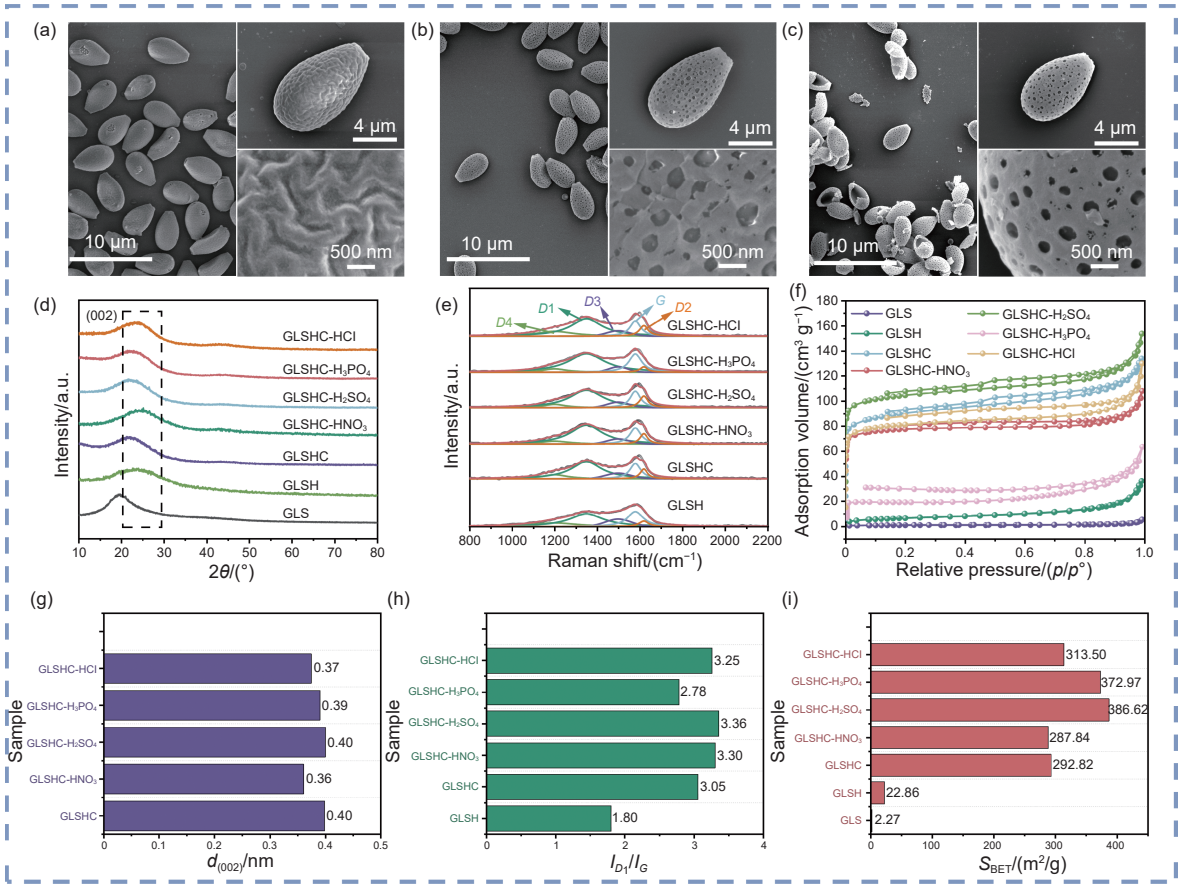

Fig. 2 Structural characterization of the prepared samples. SEM images of (a) GLS, (b) GLSH, (c) GLSHC. (d) N_2 adsorption-desorption isotherm. (e) XRD pattern. (f) Raman pattern. (g) The calculated $d_{(002)}$ interplanar spacing from (d). (h) Specific surface area. (i) Degree of graphitization I_{D1}/I_G

To clarify the structural evolution of functionalized porous spore carbon, XRD and Raman analyses were performed. It is reported that GLS are rich in chitin (~ 60%). During electrode material preparation, the chitin network molecular chains can be transformed into a hierarchical porous carbon skeleton, providing rapid ion transport pathways[38]. Pristine GLS exhibited a broad diffraction peak at 19° (Fig. 2e), arising from the chitin-β-glucan composite in the spore wall. After hydrothermal treatment (180 °C, 24 h), this peak shifted to 23° and broadened, indicating transition to an amorphous state. During hydrothermal treatment, it is hypothesized that crystalline structure is disrupted by the hydrolysis and deacetylation of chitin and other biomacromolecules[43]. Following carbonization and acid functionalization, all samples displayed broad peaks at 21°-23° corresponding to the (002) plane of nano-graphitic layers. Their calculated $d_{(002)}$ values (Fig. 2g) based on the Scherrer equation ($2d\sin\theta=n\lambda$) were larger than that of graphite (0.335 nm), indicating a more favorable condition for Na^+ insertion and extraction[44–45]. Notably, each of the following acid treatments has a distinct effect. The addition of HNO_3 or HCl induces local charge polarization, leading to layer compression under the action of strong electron-withdrawing groups, thereby resulting in a reduction in layer spacing. This structural evolution brings the carbon layer closer to a graphitized state. While enhancing the overall conductivity, it may also generate some negatively polarized regions on the surface, thereby strengthening the electrostatic adsorption effect on Na^+ and further increasing the adsorption capacity of sodium ions. Furthermore, compared with baseline GLSHC, the interlayer spacing change observed in GLSHC-HCl is relatively small, indicating that it has better retention of the layered structure. Furthermore, the HR-TEM image of GLSHC-HNO_3 (Fig. S3) reveals a hybrid morphology of amorphous domains and localized graphitic microcrystals. This observation

aligns with the corresponding diffraction pattern, confirming the disordered, defective framework characteristic of high-performance hard carbons. In contrast, the interlayer spacing of GLSHC-H_2SO_4 and GLSHC-H_3PO_4 is significantly larger than that of graphite, which may be attributed to the anchoring effect of sulfur and phosphorus elements between the carbon layers. However, excessive interlayer expansion often leads to the formation of a thicker SEI film, thereby reducing the ICE.

Raman spectra (Fig. 2f, Fig. S4a) further confirmed disorder and heterogeneity. The *G* band (1580 cm^{-1}) corresponds to the E_2g symmetric vibration of graphitic materials, reflecting crystallinity graphitic domains, while the *D*1-*D*4 bands at 1350, 1620, 1500 and 1200 cm^{-1} indicated disordered lattices (A_1g symmetry and E_2g symmetry on surface layers), amorphous carbon, and edge defects[46–47]. The I_{D1}/I_G ratio of GLSHC rose sharply to 3.05, suggesting the presence of defect-rich carbon frameworks with significant disorder. Remarkably, acid treatments are seen to further modulate disorder. Most of the acid-treated samples displayed an increased I_{D1}/I_G with the sole exception of GLSHC-H_3PO_4 (2.28), suggesting enhanced short-range ordering (Fig. 2h). This may arise from reactions between phosphoric acid and carbon layers during treatment, which suppress interlayer stacking and defect propagation and thereby improving structural order. The lateral crystallite size L_a Raman (nm) was calculated via the following formula (5):

$$L_a = \frac{2.4\times10^{-10}\times\lambda^4}{I_D/I_G} \quad (5)$$

The calculated results are displayed in Fig. S4b[48], which further corroborate the above variation trends. These results indicate that the microcrystalline size of GLSHC-HNO_3 is smaller, which can effectively increase the active sites of sodium ions. Meanwhile, thanks to the interlayer spacing close to that of graphite, HNO_3 has stronger electrical conductivity, thus being more conducive to electron transfer and improving the ICE of the material. Therefore, moderately expanding the interlayer spacing can maximize the Na^+ active site without sacrificing electrical conductivity. In this regard, GLSHC-HNO_3 struck the best balance among interlayer spacing expansion, disorder control and structural stability, laying the foundation for its superior sodium storage performance.

3.3 Doping regulation based on DFT prediction

FTIR and XPS analyses were conducted to explain the regulatory effects of acid treatments on the surface chemistry of GLSHC. It is observed by FTIR in Fig. 3a that pristine GLS contained abundant hydroxyl, carboxyl, and nitrogen groups. Hydrothermal treatment and carbonization led to cleavage of C—H bonds (2924/2856 cm^{-1}) and disappearance of the C=O peak (1740 cm^{-1}), reflecting the decomposition of fatty acids and redistribution of oxygen functionalities[49]. Subsequent acid treatments reintroduced carboxyl and carbonyl groups and tailored the surface environment. XPS further confirmed these compositional changes. Full-spectrum analysis in Fig. 3b indicates the persistent presence of N and O elements across all samples, where the regulation of heteroatom compositions is only seen in the acid-treated samples (Fig. S5). Oxygen content decreased from 25.47% (GLS) to 6.38% (GLSHC) after carbonization, but acid treatments partially restored oxygen, especially in GLSHC-HNO_3 (12.61%), consistent with the strong oxidative effect of HNO_3. Notably, nitrogen content was retained and enriched. Pristine GLSHC contained 3.34% N, sequentially rising to 6.39% (GLSHC-HNO_3), 5.01% (GLSHC-H_2SO_4), 5.31% (GLSHC-H_3PO_4) and 4.46% (GLSHC-HCl) after acid treatment, with acid functionalization stabilizing the pyridinic, pyrrolic, and graphitic N species and enhancing electronic structure and reactivity. Besides, sulfur, phosphorus, and chlorine were successfully introduced by the addition of the respective acid. Compared to the intrinsic biogenic element in GLS (S: 0.12%, P: 0.3%, Cl: 0.15%) in GLSHC, the S, P and Cl contents in GLSHC-H_2SO_4, GLSHC-H_3PO_4 and GLSHC-HCl are increased to 1.27%, 1.08% and 0.77%, respectively, confirming effective element doping. High-resolution spectra of C and N in the obtained samples are further explored (Fig. 3 and Fig. S6-S7). As for C 1s, GLSHC-HNO_3 exhibits new peaks at 285.98 eV (C—N/C—O) and 288.65 eV

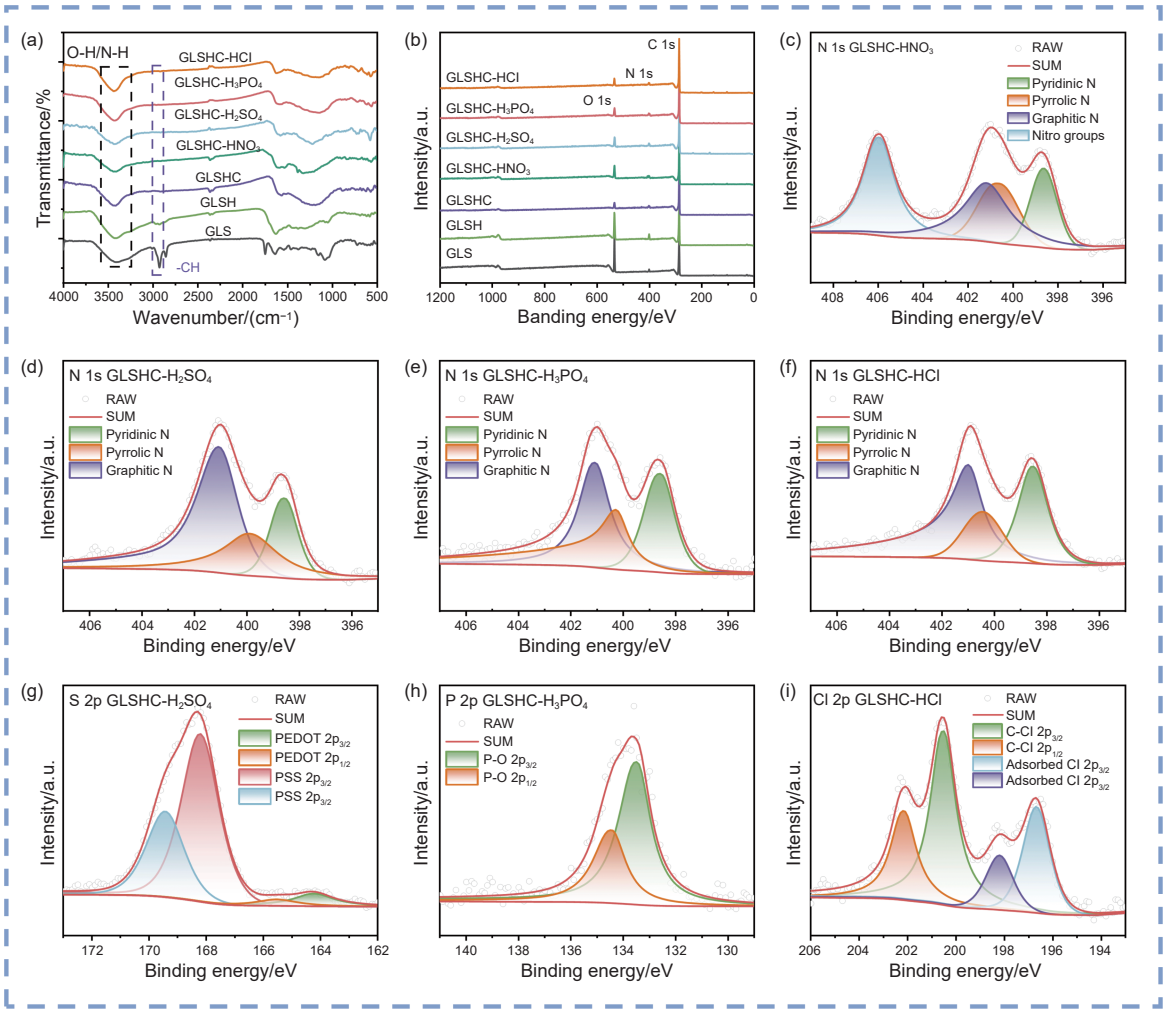

Fig. 3 Characterization of multi-doped components of HRPC. (a) FTIR spectra of GLSHC before and after functionalization. (b) XPS full spectra of GLSHC before and after functionalization. (c-f) N 1s fine spectra of GLSHC-*X* samples. (g) S 2p fine spectra of GLSHC-H_2SO_4 samples. (h) P 2p fine spectra of GLSHC-H_3PO_4 samples. (i) Cl 2p fine spectra of GLSHC-HCl samples

(O—C=O), both of which are not seen in the original GLS. Moreover, GLSHC-HNO_3 exhibited a distinct new peak at 405.92 eV indexing to nitro groups (—NO_2) (Fig. 3c), consistent with strong electron-withdrawing effects that enhance charge polarization[50]. For GLSHC-H_2SO_4, GLSHC-H_3PO_4 and GLSHC-HCl, the N 1s spectra (Fig. 3d-f) show nitrogen species similar to those of GLSHC. Additionally, GLSHC-H_2SO_4 treatment introduced sulfonic (—SO_3H) groups (Fig. 3g) at binding energies of 168.2/169.42 eV along with minor thiophene-like sulfur species (C—S) at 164.21/165.51 eV[51–52]. The presence of —SO_3H increases the binding energy of adjacent C—O bonds (286.3 eV in C 1s) due to electron cloud polarization. It enhances material hydrophilicity and electrolyte wettability, as evidenced by looking at the contact angles of electrolytes (Fig. S8). GLSHC-H_3PO_4 treatment incorporated phosphate ester bonds (—PO_4^{3-}) into the carbon framework[34] (Fig. 3h), as supported by the C 1s peak at 286.36 eV (C—O) and P 2p doublet (133.46/134.42 eV), generating crosslinking effects that suppress volume expansion and improve cycling stability. GLSHC-HCl formed covalent C—Cl bonds (Fig. 3i), creating surface carbon layer defects and polar sites beneficial for Na^+ adsorption, though excess Cl may disturb SEI formation[6]. Regardless of the treatment sequence or acid type, all acid-treated samples exhibited oxygen vacancy signals at g=2.005 (Fig. S9), which are known to optimize electronic conductivity and Na^+ storage capacity. HNO_3 treatment proves the most effective in augmenting these surface defects. In con-

trast, H_2SO_4 and HCl treatments show similar moderate improvements, whereas H_3PO_4 treatment resulted in the lowest defect density. Collectively, hydrothermal treatment, low-temperature carbonization, and acid functionalization enabled the precise regulation of surface functional groups and constructed nitrogen-doped conductive networks in GLSHC. This hybrid strategy optimized electron/ion transport, as well as generated abundant active sites, thereby enhancing Na^+ storage capacity and long-term stability.

DFT calculations were used to clarify the role of the abovementioned element doping in improving the sodium storage of HRPC. The theoretical model of HRPC is approximated using the structure of graphene to create the geometric structure models of GLSHC, GLSHC-HNO_3, GLSHC-H_2SO_4, GLSHC-H_3PO_4 and GLSHC-HCl (Fig. S10). It should be noted that the ideal graphene model simplifies the actual porous and amorphous structure of HRPC. This simplification facilitates focusing on the intrinsic effects of functional groups due to the elimination of structural variables. Although the observed values may deviate from the theory, the relative trend among different samples remains reliable for comparing Na^+ affinity. As seen from the work function calculated using the above structural models (Fig. 4a-e), the treated samples see reductions to their surface work function compared with GLSHC. GLSHC-HNO_3 exhibits the lowest work function at 4.406 eV, indicating easier surface electron transfer that accelerates interfacial electrochemical kinetics and enhances rate performance. Compared with other acid treatments, GLSHC-HNO_3 functionalization introduces higher nitrogen content and strongly polar —NO_2 groups, increasing surface electron affinity and electron density, thereby reducing the work function. The work function and Na^+ adsorption energy is intrinsically correlated through the surface electronic structure. A lower work function indicates that interfacial charge transfer and electron redistribution can occur more readily on the carbon surface, thereby strengthening the electrostatic interaction with Na^+ and resulting in a more negative adsorption energy. Adsorption energy calculations further confirm the improvement (Fig. 4f). GLSHC-HNO_3 (−4.957 eV) shows the strongest Na^+ binding affinity, followed by GLSHC-H_2SO_4 (−4.796 eV), GLSHC-H_3PO_4 (−4.712 eV), GLSHC-HCl (−4.605 eV), and pristine GLSHC (−4.597 eV), highly consistent with FTIR/XPS results. The enhanced affinity arises from the introduction of specific functional groups during acid treatment. HNO_3 treatment contributes polar oxygen-containing —NO_2 and enriched N/O sites which strengthen Na—O coordination and ionic dipole interactions. H_2SO_4 and H_3PO_4 treatments yield —SO_3H and —PO_4 groups, respectively, which polarize C—O bonds and improve Na^+ adsorption and ion transport. In contrast, HCl treatment generates C—Cl bonds and defects, which increases polarity and adsorption energy only marginally and destabilizes the SEI. Differential charge analysis (Fig. 4g) reveals the highest electron transfer (0.871 e^-) from carbon to the sodium solvate ion complex at the GLSHC-HNO_3 anode, closely aligned with the adsorption energy trend. Overall, acid functionalization enhances sodium affinity and electron transfer by synergistically combining heteroatom doping, polar oxygen-containing groups, and possible defect engineering. This improves Na^+ adsorption/nucleation, accelerates charge-transfer kinetics, and strengthens cycling stability. Notably, GLSHC-HNO_3, with its abundant N/O sites, facilitates rapid desolvation, surface migration, and uniform Na^+ intercalation, thereby achieving superior sodium storage capacity and laying a strong foundation for high-performance SICs.

3.4 Electrochemical performance

Building on the DFT insights, half-cells were assembled using HRPC as the anode, metallic sodium as both the counter and the reference electrode, to evaluate Na^+ storage behavior. Cyclic voltammetry (CV) at 0.2 mV s^{-1} within 0.01-3.0 V (vs. Na^+/Na) revealed distinct first-cycle reduction peaks for all samples (Fig. 5a), characteristic of carbon-based anodes and associated with SEI formation[53–54]. Furthermore, the surface functional group modulation by acid functionalization markedly modulated both the position and intensity of these peaks. GLSHC-HNO_3 displayed a

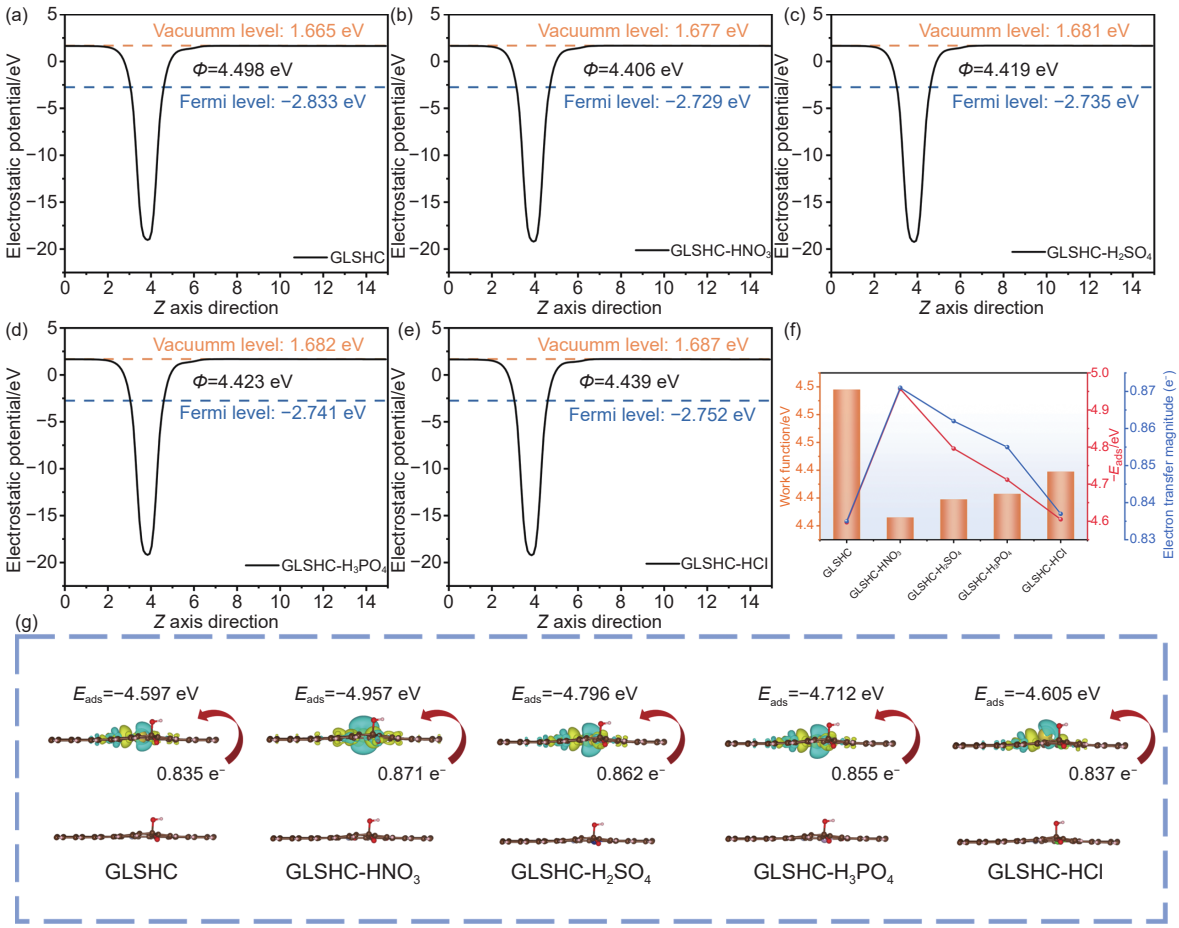

Fig. 4 Theoretical insights into HRPC anodes. Calculate the work functions of (a) GLSHC, (b) GlSHC-HNO_3, (c) GlSHC-H_2SO_4, (d) GlSHC-H_3PO_4 and (e) GLSHC-HCl. (f) The function, adsorption energy and electron transfer number of sodium ions on different HRPCs. (g) Charge density, adsorption energy and population analysis of sodium ions on HRPC

dominant reduction peak at −0.83 V with the highest current response, indicating the presence of nitro groups which promots rapid and uniform SEI formation at higher potentials, thereby minimizing electrolyte decomposition. On the contrary, GLSHC-H_2SO_4, GLSHC-HCl and GLSHC-H_3PO_4 displayed dual reduction peaks at low (0.42-0.48 V) and high (~ 0.90 V) potentials, indicative of multi-step interfacial reactions. The low-potential peaks likely originated from electrolyte reduction and defect-mediated adsorption at polar sites. These features are obviously superior to that of pristine GLSHC, the latter of which features the weakest response consistent with poor surface activity and sluggish SEI formation that may cause capacity degradation. Therefore, peak intensities can be ranked in a descending order with GLSHC-HNO_3 > GLSHC-H_2SO_4 > GLSHC-HCl > GLSHC-H_3PO_4 > GLSHC. The ranking aligns perfecrtly with decreasing oxygen content, confirming the role of heteroatom doping in enhancing interfacial kinetics. Importantly, from the second cycle onward, CV curves overlapped well for all samples, especially GLSHC-H_3PO_4 and GLSHC-H_2SO_4, indicating stabilized SEI layers and highly reversible Na^+ insertion/extraction (Fig. S11). These results demonstrate that surface functionalization not only regulates interfacial chemistry but also ensures stable long-term electrochemical performance.

Galvanostatic charge-discharge measurements (Fig. 5b) show that GLSHC-HNO_3 delivers initial discharge and charge capacities of 1023.1 and 509.1 mAh g^{-1}, respectively, showing an ICE of 49.8%, which is typical of non-graphitic carbons[55–57]. Rate performance tests (Fig. 5c) highlight its superior Na^+ storage ability, maintaining reversible capacities of 446.1, 364.0, 311.8, 293.0, 266.9, 261.5, 237.3 and

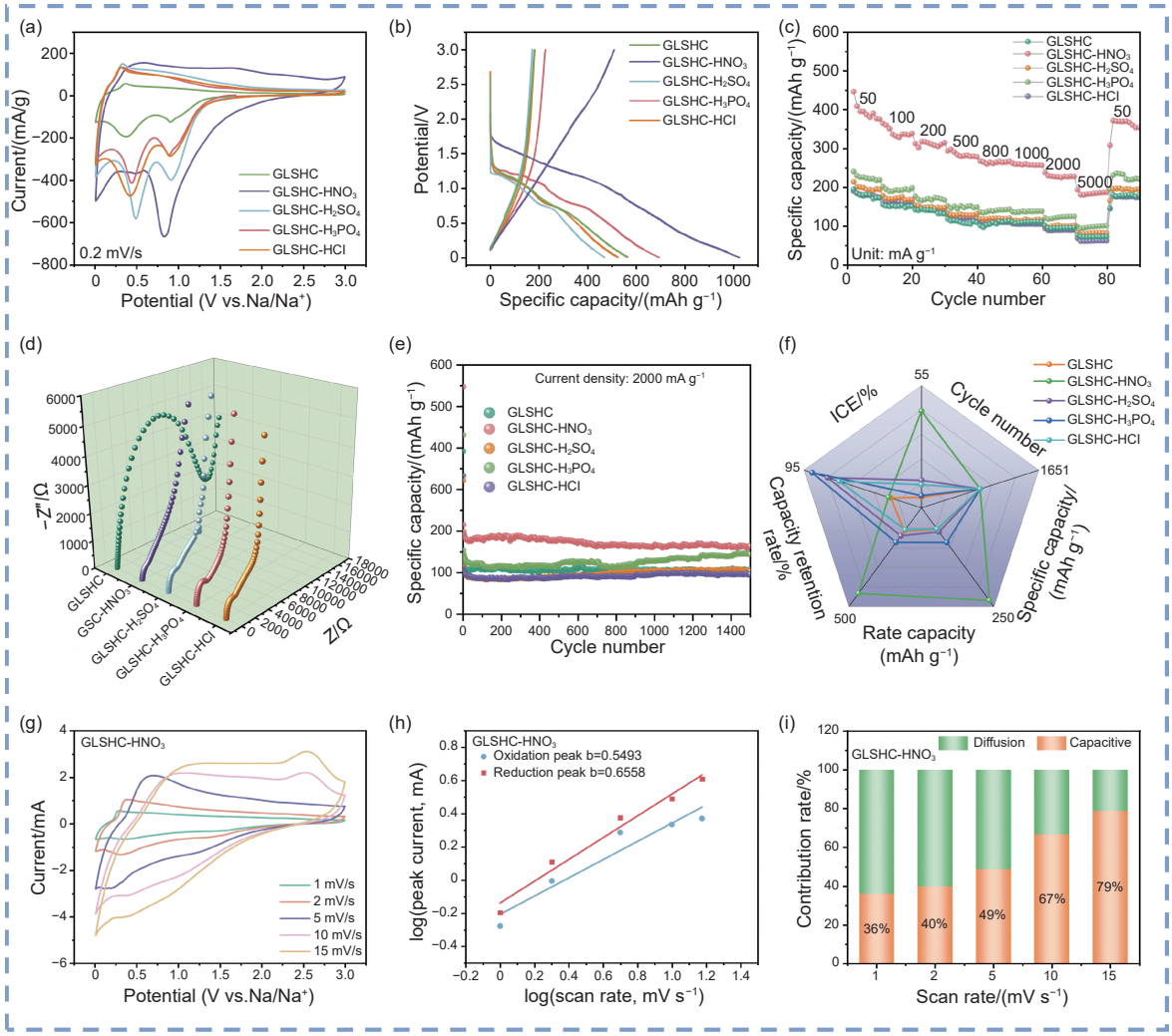

Fig. 5 Electrochemical performance of functionalized HRPC. (a) First-cycle (CV) curves of GLSHC-*X* at a scan rate of 0.2 mV s^{-1}. (b) Initial charge/discharge profiles of GLSHC-*X* at a current density of 50 mA g^{-1}. (c) Rate capability across current densities ranging from 50 to 5000 mA g^{-1}. (d) Nyquist plots of GLSHC-*X* derived from EIS in the frequency range of 100 kHz to 0.01 Hz. (e) Long-term cycling stability at 2000 mA g^{-1} for 10 000 cycles. (f) Radar plot evaluating the electrochemical properties of the HRPC electrodes. (g) CV curves of GLSHC-HNO_3 at varying scan rates (1-15 mV s^{-1}). (h) Relationship between lg(*v*) and lg(*i*) of GLSHC-HNO_3. (i) Capacitive contribution ratio of GLSHC-HNO_3 at scan rates of 1-15 mV s^{-1}, calculated using the surface-controlled and diffusion-controlled capacity separation method

192.7 mAh g^{-1} at current densities from 50 to 5000 mA g^{-1}. It should also be noted that GLSHC-HNO_3 delivers significantly higher capacities at various current rates than any other anode materials, demonstrating commendable sodium storage performance. This capability is consistent with the anticipated structural design and surface functionalization objectives. It can be attributed to the significantly enhanced charge-transfer kinetics resulting from the carbon layers being in a more graphitic state, as well as the increased Na^+ adsorption capacity provided by the highly polar oxygen-containing functional groups, further supported by the EIS analysis with a frequency range of 0.01-100 kHz (Fig. 5d). Thanks to the stabilization of the SEI and carbon skeleton by phosphate ester crosslinking and sulfonic acid group modification, continuous activation and long cycle performance were achieved. GLSHC-H_3PO_4 and GLSHC-H_2SO_4 exhibited superior capacity retention rates after 1500 cycles at a high current density (2000 mA g^{-1}) (Fig. 5e). Furthermore, after 1500 cycles at a current density of 2000 mA g^{-1}, the HRPC electrode still maintained its original droplet-like shape with no obvious cracks, pore collapse or pulverization on the surface (Fig. S12), indicating excellent mechanical strength of the porous carbon framework. GLSHC-

HNO_3 achieved a circulating capacity retention rate of 80.6% while maintaining a higher capacity. Its cycling performance compared with other carbon-based materials is shown in Table S1. Fig. 5f compares the electrochemical performance of different HRPCs, demonstrating the superior performance of the GLSHC-HNO_3 electrode in terms of ICE, cycle number, specific capacity, cycle capacity retention rate and rate capacity. To gain greater insight into the charge storage kinetics of GLSHC-HNO_3, CVs of GLSHC-HNO_3 are given in Fig. 5g. The relationship between current (i, mA) and scan rate (v, mV s^{-1}) follows Eq. (6)[52,58]:

$$i = ab^v \quad (6)$$

where a is a constant and b characterizes the electrochemical behavior. A b-value approaching 0.5 suggests diffusion-controlled processes, while b≈1 indicates surface-limited pseudocapacitive dominance. The fitted b-values indicate distinct storage mechanisms.

GLSHC-H_2SO_4 and GLSHC-H_3PO_4 have the b-values of 0.83/1.01 (anode/cathode) and 0.80/0.97 (anode/cathode), exhibiting pseudocapacitive-dominated processes that are ideal for high-rate performance (Fig. S13), while GLSHC-HNO_3 possesses b-values of 0.55/0.66 (anode/cathode) (Fig. 5i), reflecting diffusion-controlled kinetics due to hindered ion migration caused by dense polar groups. Both untreated and HCl-treated GLSHC show intermediate b-values between 0.5 and 1, indicating mixed control. This suggests that sodium storage is governed by a combination of surface adsorption and diffusion, offering moderate reactivity but limited rate capability. The capacity contribution ratio was further quantified using the following Eq. (7)[59–60]:

$$i(V) = k_1 v + k_2 v^{1/2} \quad (7)$$

where $k_1 v$ and $k_2 v^{1/2}$ represent capacitive and diffusion-controlled contributions, respectively. As shown in Fig. 5h, GLSHC-HNO_3 displays low pseudocapacitance (36%-79%) dominated by diffusion processes, limited by excessive SEI formation and passivation induced by —COOH, C=O and —NO_2 groups, consistent with DFT predictions. Conversely, other functionalized samples demonstrated superior capacitive dominance (Fig. S13). GLSHC-H_2SO_4 achieves the highest capacitive contribution (60%-94%), benefiting from —SO_3H/C—S functionalities which accelerate electron transfer and Na^+ adsorption. GLSHC-H_3PO_4 also delivers a high capacitive contribution of 61%-94%, achieving balanced pseudocapacitive storage by C=O=P crosslinking. Besides, GLSHC-HCl gradually activates Cl-induced defects, increasing capacitive behavior from 52% to 91% with scan rate rising. Collectively, these results highlight that tailored acid functionalization not only modulates Na^+ storage mechanisms but also achieves a balance between interfacial stability, pseudocapacitance, and long-term cyclability, which is key for advancing high-performance SIC anodes.

3.5 SICs performance

To evaluate the practical application potential of HRPC in SICs, we assembled a full-cell configuration employing GLSHC-HNO_3 as the anode and PDPC as the cathode with $NaClO_4$-based organic electrolyte (schematic illustration in Fig. 6a). GLSHC-HNO_3 was selected as the anode due to its exceptionally high initial discharge capacity (exceeding 1000 mAh g^{-1}), coupled with reversible capacity and excellent performance at high rates. Even under an ultrahigh current density of 5000 mA g^{-1}, it maintains a capacity close to 200 mAh g^{-1}, which is conducive to achieving high energy density in SICs. For the cathode, PDPC exhibits stable operating characteristics within the voltage range of 3.0-4.2 V (vs. Na/Na^+), delivering a specific capacity of 41 mAh g^{-1} at 100 mA g^{-1} and excellent rate performance (Fig. S14). Considering the compatibility of the potential windows of both electrodes, the theoretical cell voltage could reach up to 4.1 V. To mitigate the risks associated with electrolyte decomposition and other side reactions, the practical operating voltage window of the full cell was set to 2.0-3.8 V. To achieve charge balance, a mass matching was conducted based on the actual capacities of the positive and negative electrodes at a current density of 2000 mA g^{-1}. The reversible specific capacity of the GLSHC-HNO_3 negative electrode is approximately 237.3 mAh g^{-1}, while the spe-

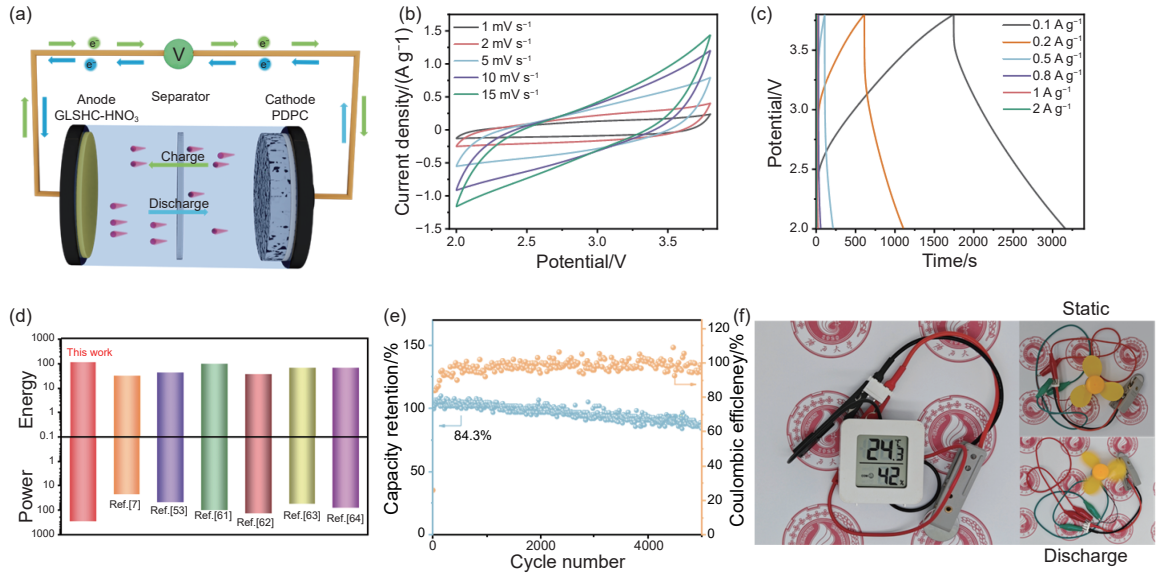

Fig. 6 Electrochemical performance of the assembled SIC with GLSHC-HNO_3 anode and PDPC cathode within a 2.0-4.0 V operating voltage window. (a) Conceptual drawing of GLSHC-HNO_3 capacitor. (b) CV curves at scan rates of 1, 2, 5, 10 and 15 mV s^{-1}. (c) GCD profiles at current densities of 0.1, 0.2, 0.5, 0.8, 1.0 and 2.0 A g^{-1}. (d) Comparison of energy and power density of different Na-ion capacitor. (e) Cycling stability and coulombic efficiency at 2.0 A g^{-1}. (f) SiC drives the thermometer and hygrometer and the electric fan

cific capacity of the PDPC positive electrode is approximately 32.2 mAh g^{-1}. According to the charge balance relationship ($m_{anode}/m_{cathode}=C_{cathode}/C_{anode}$), the anode:cathode mass ratio is approximately 1 : 7. As shown in Fig. 6b, the GLSHC-HNO_3//PDPC full cell delivered nearly rectangular CV curves, maintaining a good symmetry even at high scan rates (1-15 mV s^{-1}), indicative of excellent reversibility and rapid ion/electron transport. GCD profiles (Fig. 6c) further confirmed efficient charge-discharge behavior. The resulting device achieved an impressive energy density of 114.4 Wh kg^{-1} at a power density of 290 W kg^{-1}, retaining 43.1 Wh kg^{-1} at 1450 W kg^{-1}, with a maximum power output of 5800 W kg^{-1}. Notably, compared with representative SIC systems, it shows higher power and energy density (Fig. 6d and Fig. S15)[7,53,61–64], maintaining a gentle energy decay across a wide power range, reflecting outstanding rate performance. After 5000 charge-discharge cycles at a current density of 2.0 A g^{-1}, the capacity retention rate of this device remaiend highly (84.3%). The Coulomb efficiency rose rapidly to approximately 83.9% in the first few cycles and remained close to 100% throughout the subsequent cycles (Fig. 6e), indicating its excellent long-term stability and reversibility. Practical applicability was further validated by powering small electronic devices such as a thermometer, a hygrometer, and a mini-fan (Fig. 6f), underscoring the strong potential of GLSHC-HNO_3//PDPC SICs for high-performance energy storage applications.

4 Conclusion

In summary, this work demonstrated a sustainable fabrication strategy for high-performance SICs using HRPC-derived from biomass. By integrating hydrothermal treatment, low-temperature carbonization, and acid-mediated functionalization, GLSHC-HNO_3 anodes with hierarchical porosity and multi-element co-doping were successfully developed, superior to all other acid-treated samples. Coupled with PDPC cathodes, the assembled full cell delivered an exceptional energy density of 114.4 Wh kg^{-1} at 290 W kg^{-1}, 43.1 Wh kg^{-1} at 1450 W kg^{-1}, and achieving a maximum power density of 5800 W kg^{-1}. In the long term, 84.3% of capacity and nearly 100% of Coulombic efficiency were retained after 5000 cycles. Compared with reported works, the device exhibits superior energy output, rate capability, and cycling stability. This study not only provides a green and scalable approach for utilizing biomass in the synthesis of advanced biochars but also establishes a valu-

able design framework for optimizing carbon-based electrodes in next-generation SICs.

References

[1] Gupta S, Carrizosa S B, Aberg B. Designing high-performance asymmetric and hybrid energy devices via merging supercapacitive/pseudopcapacitive and Li-ion battery type electrodes[J]. Scientific Reports, 2024, 14(1): 29277.

[2] Salanne M, Rotenberg B, Naoi K, et al. Efficient storage mechanisms for building better supercapacitors[J]. Nature Energy, 2016, 1(6): 16070.

[3] Liang J, Wang D W. Design rationale and device configuration of lithium-ion capacitors[J]. Advanced Energy Materials, 2022, 12(25): 2200920.

[4] Hu X, Wang G X, Li J W, et al. Significant contribution of single atomic Mn implanted in carbon nanosheets to high-performance sodium-ion hybrid capacitors[J]. Energy & Environmental Science, 2021, 14(8): 4564-4573.

[5] Amatucci G G, Badway F, Du Pasquier A, et al. An asymmetric hybrid Nonaqueous energy storage cell[J]. Journal of The Electrochemical Society, 2001, 148(8): A930.

[6] Zhang Y, Jiang J, An Y, et al. Sodium-ion capacitors: materials, mechanism, and challenges[J]. ChemSusChem, 2020, 13(10): 2522-2539.

[7] Wang R, Wang S, Peng X, et al. Elucidating the intercalation pseudocapacitance mechanism of MoS_2-carbon monolayer interoverlapped superstructure: toward high-performance sodium-ion-based hybrid supercapacitor[J]. ACS Applied Materials & Interfaces, 2017, 9(38): 32745-32755.

[8] Wang L, Hu M, Yao Q, et al. Advanced materials for sodium-ion capacitors: Progress and perspectives[J]. Energy Storage Materials, 2025, 78: 104285.

[9] Ding J, Wang H L, Li Z, et al. Peanut shell hybrid sodium ion capacitor with extreme energy-power rivals lithium ion capacitors[J]. Energy & Environmental Science, 2015, 8(3): 941-955.

[10] Zhang H Z, Chen C, Xu H, et al. Hard carbon derived from straw as anode materials for sodium-ion batteries[J]. International Journal of Electrochemical Science, 2022, 17(11): 221113.

[11] Kydyrbayeva U, Baltash Y, Mukhan O, et al. The buckwheat-derived hard carbon as an anode material for sodium-ion energy storage system[J]. Journal of Energy Storage, 2024, 96: 112629.

[12] Feng B, Xu L Q, Yu Z Y, et al. Wood-derived carbon anode for sodium-ion batteries[J]. Electrochemistry Communications , 2023, 148: 107439.

[13] Mohanty A K, Vivekanandhan S, Das O, et al. Biocarbon materials[J]. Nature Reviews Methods Primers, 2024, 4(1): 19.

[14] Zhu Z, Men Y, Zhang W, et al. Versatile carbon-based materials from biomass for advanced electrochemical energy storage systems[J]. eScience, 2024, 4(5): 100249.

[15] Stevens D A, Dahn J R. High capacity anode materials for rechargeable sodium-ion batteries[J]. Journal of The Electrochemical Society, 2000, 147(4): 1271.

[16] Gao Y, Xing Y, Jiao Y, et al. High performance spherical hard carbon anodes for Na-ion batteries derived from starch-rich longan kernel[J]. Journal of Energy Storage, 2024, 98: 113167.

[17] Hou Z, Lei D, Jiang M, et al. Biomass-derived hard carbon with interlayer spacing optimization toward ultrastable Na-ion storage[J]. ACS Applied Materials & Interfaces, 2023, 15(1): 1367-1375.

[18] Dong S, He X J, Zhang H F, et al. Surface modification of biomass-derived hard carbon by grafting porous carbon nanosheets for high-performance supercapacitors[J]. Journal of Materials Chemistry A, 2018, 6(33): 15954-15960.

[19] Peng J, Huang T, Li B, et al. Mercerization-enhanced cellulose-II cotton fiber-based low-temperature hard carbon for sodium-ion batteries[J]. Industrial Crops and Products, 2024, 222: 119511.

[20] Dubey P, Shrivastav V, Maheshwari P H, et al. Recent advances in biomass derived activated carbon electrodes for hybrid electrochemical capacitor applications: challenges and opportunities[J]. Carbon, 2020, 170: 1-29.

[21] Shen S, Zhou R, Li Y, et al. Bacterium, fungus, and virus microorganisms for energy storage and conversion[J]. Small Methods, 2019, 3(12): 1900596.

[22] Cui J, Liu J, Chen X, et al. Ganoderma lucidum-derived erythrocyte-like sustainable materials[J]. Carbon, 2022, 196: 70-77.

[23] Jia S, Zhang B, Gao J, et al. Biomass-derived hard carbon anodes: From structural engineering to industrial sodium-ion battery applications[J]. Energy Storage Materials, 2025, 80: 104420.

[24] Pei Z, Meng Q, Wei L, et al. Toward efficient and high rate sodium-ion storage: a new insight from dopant-defect interplay in textured carbon anode materials[J]. Energy Storage Materials, 2020, 28: 55-63.

[25] Li M, Li Z, Bai F, et al. Multitrack boosted hard carbon anodes: innovative paths and advanced performances in sodium-ion batteries[J]. Small, 2025, 21(17): 2500645.

[26] Zhang P, Shu Y R, Zhong B H, et al. Optimizing sodium storage mechanisms and electrochemical performance of high nitrogen-doped hard carbon anode materials derived from waste plastics for sodium-ion batteries[J]. Chemical Engineering Journal, 2024, 498: 155231.

[27] Qiu D, Zhang B, Zhang T, et al. Sulfur-doped carbon for potassium-ion battery anode: insight into the doping and potassium storage mechanism of sulfur[J]. ACS Nano, 2022, 16(12): 21443-21451.

[28] Lu M, Yu W, Shi J, et al. Self-doped carbon architectures with heteroatoms containing nitrogen, oxygen and sulfur as high-performance anodes for lithium- and sodium-ion batteries[J]. Electrochimica Acta, 2017, 251: 396-406.

[29] Li Y, Yuan Y, Bai Y, et al. Insights into the Na^+ storage mechanism of phosphorus-functionalized hard carbon as ultrahigh capacity anodes[J]. Advanced Energy Materials, 2018, 8(18): 1702781.

[30] Liu B, Hou J, Wang K, et al. Surface charge regulation of graphene by fluorine and chlorine co-doping for constructing ultra-stable and large energy density micro-supercapacitors[J]. Advanced Science, 2024, 11(42): 2402033.

[31] Jin Q, Wang K, Feng P, et al. Surface-dominated storage of heteroatoms-doping hard carbon for sodium-ion batteries[J]. Energy Storage Materials, 2020, 27: 43-50.

[32] Sun D, Tang C, Cheng H, et al. Pumpkin-like MoP-MoS_2@Aspergillus niger spore-derived N-doped carbon heterostructure for enhanced potassium storage[J]. Journal of Energy Chemistry, 2022, 72: 479-486.

[33] Yang M, Dai J, He M, et al. Biomass-derived carbon from Ganoderma lucidum spore as a promising anode material for rapid potassium-ion storage[J]. Journal of Colloid and Interface Science, 2020, 567: 256-263.

[34] Zhong Y, Xia X, Deng S, et al. Spore carbon from aspergillus oryzae for advanced electrochemical energy storage[J]. Advanced Materials, 2018, 30(46): 1805165.

[35] Zhang Y, Yan K, Ji F, et al. Enhanced removal of toxic heavy metals using swarming biohybrid adsorbents[J]. Advanced Functional Materials, 2018, 28(52): 1806340.

[36] Zhang Y, Chan K F, Wang B, et al. Spore-derived color-tunable multi-doped carbon nanodots as sensitive nanosensors and intracellular imaging agents[J]. Sensors and Actuators B: Chemical, 2018, 271: 128-136.

[37] Wang X, Yu H, Xia X, et al. Scalable fabrication of biohybrid magnetic MOF-based micromotors for toxin enrichment[J]. Journal of Colloid and Interface Science, 2025, 683: 27-38.

[38] Wang Y, Liu R, Tian Y, et al. Heteroatoms-doped hierarchical porous carbon derived from chitin for flexible all-solid-state symmetric supercapacitors[J]. Chemical Engineering Journal, 2020, 384: 123263.

[39] Ma J, Fu Z, Ma P, et al. Breaking and characteristics of Ganoderma lucidum spores by high speed entrifugal shearing pulverizer[J]. Journal of Wuhan University of Technology-Materials Science Edition, 2007, 22(4): 617-621.

[40] Liu Y, Hu S, Hu T, et al. Fabrication of oxygen-rich/nitrogen-doped hierarchical porous Ganoderma lucidum spore activated carbon for enhanced supercapacitor performance[J]. Journal of Materials Science, 2024, 59(32): 15315-15329.

[41] Bailey S E, Olin T J, Bricka R M, et al. A review of potentially low-cost sorbents for heavy metals[J]. Water Research, 1999, 33(11): 2469-2479.

[42] Sakanishi K, Ikeyama N, Sakaki T, et al. Comparison of the hydrothermal decomposition reactivities of chitin and cellulose[J]. Industrial & Engineering Chemistry Research, 1999, 38(6): 2177-2181.

[43] Zhu L F, Yao Z C, Ahmad Z, et al. Synthesis and evaluation of herbal chitosan from Ganoderma lucidum spore powder for biomedical applications[J]. Scientific Reports, 2018, 8(1): 14608.

[44] Tang K, Fu L, White R J, et al. Hollow carbon nanospheres with superior rate capability for sodium-based batteries[J]. Advanced Energy Materials, 2012, 2(7): 873-877.

[45] Mahmood A, Yuan Z, Sui X, et al. Foldable and scrollable graphene paper with tuned interlayer spacing as high areal capacity anodes for sodium-ion batteries[J]. Energy Storage Materials, 2021, 41: 395-403.

[46] Rantitsch G, Bhattacharyya A, Schenk J, et al. Assessing the quality of metallurgical coke by Raman spectroscopy[J]. International Journal of Coal Geology, 2014, 130: 1-7.

[47] Morga R. Micro-Raman spectroscopy of carbonized semifusinite and fusinite[J]. International Journal of Coal Geology, 2011, 87(3): 253-267.

[48] Cançado L G, Takai K, Enoki T, et al. General equation for the determination of the crystallite size La of nanographite by Raman spectroscopy[J]. Applied Physics Letters, 2006, 88(16): 163106.

[49] Qiao J, Li J, Liu C, et al. Efficient detection technology of Ganoderma lucidum spore powder quality based on electronic nose[J]. Chemical Engineering Journal, 2025, 511: 162158.

[50] Cui J, Li W, Su P, et al. Repair surface defects on biomass derived hard carbon anodes with N-doped soft carbon to boost performance for sodium-ion batteries[J]. Advanced Energy Materials, 2025, 15: 2502082.

[51] Tan N, Zhao L, Weng Y, et al. Biomass-derived carbon materials for smart electronics: insights from wood pitch-based microsupercapacitors[J]. Advanced Functional Materials, 2024, 35(1): 2411596.

[52] Li Y, Ni B, Li X, et al. High-performance Na-ion storage of S-doped porous carbon derived from conjugated microporous polymers[J]. Nano-Micro Letters, 2019, 11(1): 60.

[53] Wang S, Wang R, Zhang Y, et al. Scalable and sustainable synthesis of carbon microspheres via a purification-free strategy for sodium-ion capacitors[J]. Journal of Power Sources, 2018, 379: 33-40.

[54] Li Y, Hu Y S, Titirici M M, et al. Hard carbon microtubes made from renewable cotton as high-performance anode material for sodium-ion batteries[J]. Advanced Energy Materials, 2016, 6(18): 1600659.

[55] Gaddam R R, Yang D, Narayan R, et al. Biomass derived carbon nanoparticle as anodes for high performance sodium and lithium ion batteries[J]. Nano Energy, 2016, 26: 346-352.

[56] Selvamani V, Ravikumar R, Suryanarayanan V, et al. Garlic peel derived high capacity hierarchical N-doped porous carbon anode for sodium/lithium ion cell[J]. Electrochimica Acta, 2016, 190: 337-345.

[57] Fonseca W S, Meng X, Deng D. Trash to treasure: transforming waste polystyrene cups into negative electrode materials for sodium ion batteries[J]. ACS Sustainable Chemistry & Engineering, 2015, 3(9): 2153-2159.

[58] Chao D, Liang P, Chen Z, et al. Pseudocapacitive Na-ion storage boosts high rate and areal capacity of self-branched 2D layered metal chalcogenide nanoarrays[J]. ACS Nano, 2016, 10(11): 10211-10219.

[59] Zhao C, Yu C, Zhang M, et al. Ultrafine MoO_2-carbon microstructures enable ultralong-life power-type sodium ion storage by enhanced pseudocapacitance[J]. Advanced Energy Materials, 2017, 7(15): 1602880.

[60] Brezesinski T, Wang J, Tolbert S H, et al. Ordered mesoporous α-MoO_3 with iso-oriented nanocrystalline walls for thin-film pseudocapacitors[J]. Nature Materials, 2010, 9(2): 146-151.

[61] Chen Z, Augustyn V, Jia X, et al. High-performance sodium-ion pseudocapacitors based on hierarchically porous nanowire composites[J]. ACS Nano, 2012, 6(5): 4319-4327.

［62］ Kim M S, Lim E, Kim S, et al. General synthesis of N-doped macroporous graphene-encapsulated mesoporous metal oxides and their application as new anode materials for sodium-ion hybrid supercapacitors[J]. Advanced Functional Materials, 2017, 27(3): 1603921.

［63］ Liu Z, Cao Y, Zhang H, et al. Low-cost, high-energy Na-ion hybrid supercapacitors[J]. ACS Sustainable Chemistry & Engineering, 2022, 10(32): 10675-10684.

［64］ Jian Z, Raju V, Li Z, et al. A high-power symmetric Na-ion pseudocapacitor[J]. Advanced Functional Materials, 2015, 25(36): 5778-5785.